Mode-1 N_2 internal tides observed by satellite altimetry

Zhongxiang Zhao[1]

[1]Applied Physics Laboratory and School of Oceanography, University of Washington, Seattle, Washington, USA

Correspondence: Zhongxiang Zhao (zzhao@uw.edu)

Abstract. Satellite altimetry provides a unique technique for observing the sea surface height (SSH) signature of internal tides from space. Previous studies have constructed empirical internal tide models for the largest four tidal constituents M_2, S_2, K_1, and O_1 by satellite altimetry. However, no empirical internal tide models have been constructed for minor constituents yet. In this study, we observe mode-1 N_2 internal tides, the fifth largest oceanic tidal constituent, using about 100 satellite-years of SSH data from 1993 to 2019. We employ a newly-developed mapping procedure that includes two rounds of plane wave analysis and a two-dimensional bandpass filter in between. We find that mode-1 N_2 internal tides have mm-scale SSH amplitudes. Model errors are estimated using 13 sets of background internal tides between N_2 and M_2. The new mode-1 N_2 internal tide model is evaluated using independent satellite SSH data in 2020 and 2021. Our observations show that the N_2 and M_2 internal tides have similar spatial patterns, and that the N_2 amplitudes are about 20% of the M_2 amplitudes. The mode-1 N_2 internal tides are observed to propagate hundreds to thousands of kilometers in the open ocean. Our work demonstrates that minor internal tidal constituents can be observed using multiyear multisatellite data and new mapping techniques. Our mode-1 N_2 model can make internal tide correction for SWOT, and inversely the new SWOT data can improve internal tide models of minor tidal constituents and higher baroclinic modes.

1 Introduction

The Moon's elliptical orbit around the Earth has an eccentricity of $\approx$0.055, with its perigean and apogean distances being about 3.63×10^5 and 4.06×10^5 km, respectively. The Moon completes one revolution every 27.5546 days (one anomalistic month). The tidal constituents L_2 and N_2 are induced by the Moon's elliptical orbit (Doodson, 1921). They are named the smaller and larger lunar elliptical semidiurnal constituents. The L_2 and N_2 periods are 12.1916 and 12.6583 hours, respectively (Doodson, 1921; Pawlowicz et al., 2002). M_2 (12.4206 hours) is based on the mean distance between the Earth and the Moon (3.84×10^5 km). While the L_2 and N_2 superposition gives the 27.5546-day perturbation with the Moon-Earth distance changes along the elliptic orbit. On global average, the amplitudes of M_2, N_2, and L_2 have a respective ratio of $1 : 0.2 : 0.05$. N_2 is the fifth largest tidal constituent; therefore, its impact on the ocean environment is significant. For example, in waters around New Zealand, the N_2 barotropic tide has larger amplitudes than S_2 (Byun and Hart, 2020, Figure 4 therein). The superposition of N_2, M_2, L_2, and S_2 can cause perigean spring tides (king tides) and apogean neap tides, which significantly affect harbors, coastal regions, and estuaries (Wood, 1978). Including N_2 internal tides can describe the temporal variation of internal tide-driven ocean mixing with the Moon's elliptical motion.

Internal tides are widespread in the ocean and affect numerous ocean processes such as diapycnal mixing, tracer transport and acoustic transmission (Wunsch, 1975; Dushaw et al., 1995; Whalen et al., 2020). Internal tides provide about half of the power for diapycnal mixing in the ocean interior (Munk and Wunsch, 1998; Egbert and Ray, 2000; MacKinnon et al., 2017; Kelly et al., 2021). The magnitude and geography of diapycnal mixing modulate the large-scale ocean circulation and global climate change; therefore, it is important to study their generation, propagation, and dissipation in the global ocean (Jayne and St. Laurent, 2001; Melet et al., 2016; Pollmann et al., 2019; Vic et al., 2019; de Lavergne et al., 2020; Arbic, 2022). Internal tides are annoying noise in the study of mesoscale and sub-mesoscale dynamics. In particular, it is necessary to make internal tide correction to the Surface Water and Ocean Topography (SWOT) data, so that one can better study the sub-mesoscale dynamic processes (Fu and Ubelmann, 2014; Qiu et al., 2018; Wang et al., 2018; Morrow et al., 2019). Empirical internal tide models can be constructed using past satellite altimetry sea surface height (SSH) measurements. However, previous satellite observations focus mainly on the largest four tidal constituents M_2, S_2, K_1, and O_1 (Dushaw, 2015; Ray and Zaron, 2016; Zhao et al., 2016; Zaron, 2019; Ubelmann et al., 2022). Dushaw (2015) attempts to map N_2 internal tides using the TOPEX/Poseidon data from 1992 to 2008, but fails to obtain an empirical model because the resulting N_2 internal tides are too noisy (see his Figures 38 and 52). That work is mainly limited by the short data set available then. In this study, we will construct a reliable empirical N_2 internal tide model using a larger data set and a new mapping method.

The challenge of observing N_2 internal tides by satellite altimetry lies in their small SSH displacements (Dushaw, 2015). Given that M_2 internal tides have SSH amplitudes of 1–2 cm, N_2 internal tides have only sub-centimeter SSH amplitudes. In this paper, the observation of N_2 internal tides is made possible by two improvements. First, a larger SSH data set becomes available, thanks to 27 years of multiple satellite missions from 1993 to 2019. The merged SSH data set is about 100 satellite-years long; therefore, nontidal errors can be significantly suppressed. Second, a newly-developed mapping procedure is employed. This mapping technique extracts N_2 internal tides utilizing their known frequency and theoretical wavelengths. Nontidal errors can be significantly suppressed by both temporal and spatial filtering. The resulting N_2 internal tides reveal their basic features in the global ocean, although they are still noisy (compared to M_2 internal tides). It is challenging (though possible) to extract L_2 internal tides, which are estimated to have 1-mm SSH signals at most (5% of M_2).

The rest of this paper is arranged as follows. Section 2 describes the data and methods used in this paper. Section 3 presents and discusses the new N_2 internal tides, mainly by comparing with the well-studied M_2 internal tides. Section 4 is a summary.

2 Data and methods

2.1 Data

The satellite altimetry SSH data used in this paper are collected by multiple altimetry missions from 1993 to 2019. In the order of launch time, they are TOPEX/Poseidon, ERS-1, ERS-2, Geosat Follow-On, Jason-1, Envisat, Jason-2, CryoSat-2, SARAL/AltiKa, Haiyang-2A, Sentinel-3A, Sentinel-3B, Haiyang-2B and Jason-CS/Sentinel-6 (Figure 1). The combined data set is about 100 satellite-years long. We use the satellite along-track SSH data downloaded from the Copernicus Marine Service (https://doi.org/10.48670/moi-00146). The SSH measurements have been processed by standard corrections for atmospheric
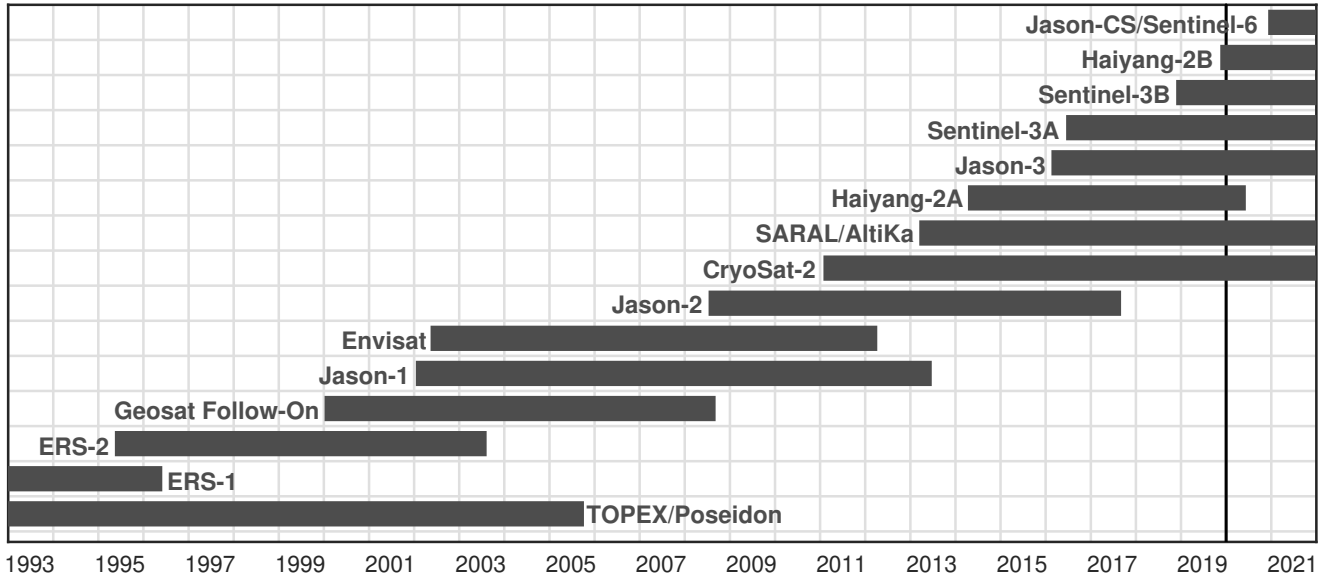
Figure 1. Satellite altimetry data used in this study. The merged multiyear multisatellite data from 1993 to 2019 are about 100 satellite-years long. The data in 2020 and 2021 work as independent data for model evaluation.

effects, surface wave bias, and geophysical effects (Pujol et al., 2016; Taburet et al., 2019). The ocean barotropic tide, polar tide, solid Earth tide and loading tide are corrected using theoretical or empirical models (Pujol et al., 2016). Mesoscale correction (Ray and Byrne, 2010; Zhao, 2022a) is made using the gridded SSH fields downloaded from the Copernicus Marine Service (https://doi.org/10.48670/moi-00148). The satellite along-track SSH data in 2020 and 2021 are used to evaluate the new N_2 internal tide model as independent data (Section 2.6). Using the multiyear combined data, our N_2 internal tide model contain only the 27-year-coherent component.

The observation of internal tides by satellite altimetry may be affected by an issue called tidal aliasing, because the repeat cycles of satellites are much longer than the semidiurnal and diurnal tides. Here we examine possible tidal aliasing issues with N_2 and M_2 internal tides. In one 160 km by 160 km fitting window (section 2.2), there are typically about 7.84×10^4 SSH data from multiyear multisatellite measurements. Using their observation times, we can calculate their phase lags with respect to the N_2 tidal cycle (12.6583 hours). Figure 2a gives the histogram of their phase lags over one N_2 tidal cycle. For comparison, Figure 2b shows the histogram with respect to one M_2 tidal cycle (12.4206 hours). The results show that the SSH data overall evenly distribute over one N_2 or M_2 tidal cycle, without extreme biases. In particular, their distribution on M_2 is smooth, suggesting that there is no tidal aliasing problem for M_2. Their distribution on N_2 is a little bumpy, suggesting that the resulting N_2 internal tides may have larger errors. The uneven distribution stems from the orbital configurations of the satellite missions. Fortunately, as shown in this study, the resultant mode-1 N_2 internal tides can overcome background errors.
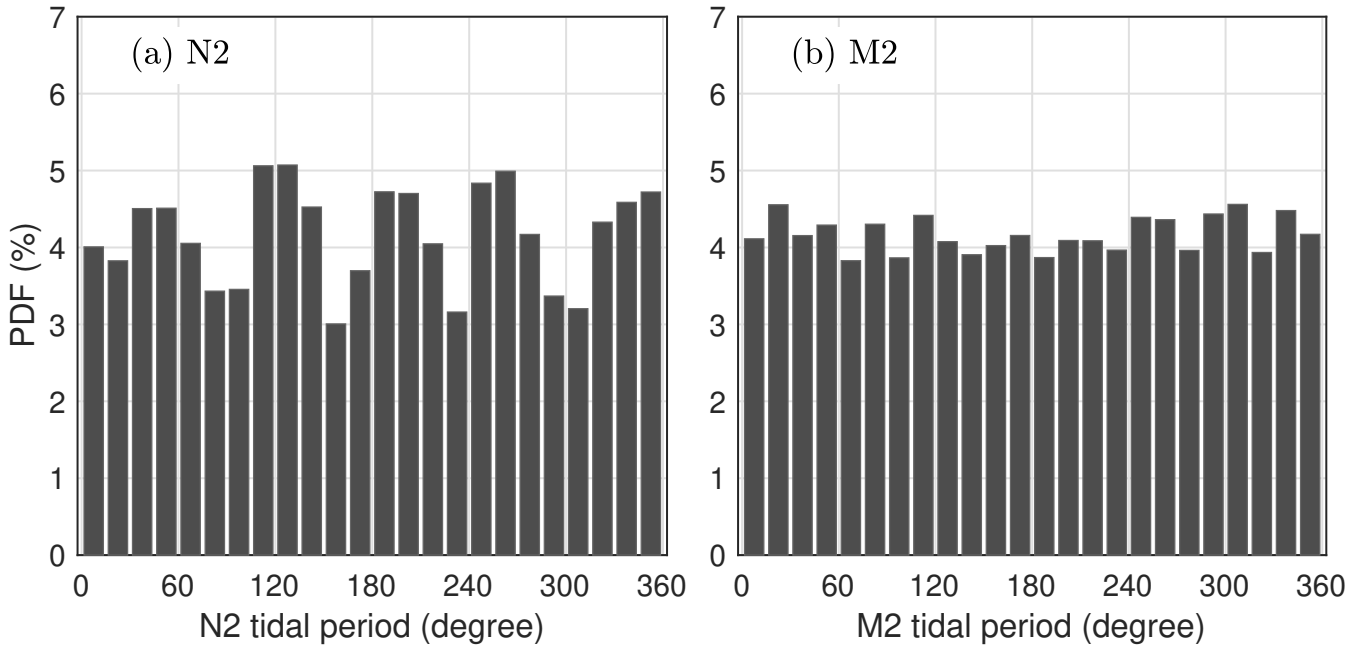
Figure 2. Histograms of the phase lags of the satellite SSH data over one N_2 (a) and M_2 (b) tidal period. This example is for one 160 km by 160 km window centered at 15°N, 160°W. There are about 7.84×10^4 SSH measurements in this window. From their observation times, the phase lags with respect to N_2 and M_2 are calculated.

2.2 Plane wave analysis

The core technique of our new mapping procedure is plane wave analysis. By this method, internal tides are determined by fitting horizontal plane waves in one given fitting window (160 km by 160 km in this study), in contrast to harmonic analysis at one single site. This method has been described in detail in our previous studies (Zhao and Alford, 2009; Zhao, 2014; Zhao et al., 2016). For each tidal constituent, there may be multiple internal tides of arbitrary propagation directions at each site, due to their multiple source regions and long-range propagation. Plane wave analysis can resolve these internal tides by propagation direction. We will fit 5 mode-1 N_2 internal tidal waves at each site. Our 5-wave representor follows

$$\Sigma_{m=1}^{5} A_m \cos(k\,x\cos\theta_m + k\,y\sin\theta_m - \omega\,t - \phi_m), \tag{1}$$

where x and y are the east and north Cartesian coordinates, t is time, ω and k are the frequency and horizontal wavenumber of the target internal tides, respectively. Three parameters need to be determined for each internal tidal wave: amplitude A, phase ϕ, and direction θ. To determine one wave, the amplitude and phase of a single plane wave are determined by the least-squares fit in each compass direction (with 1° increment). When the resultant amplitudes are plotted as a function of direction in polar coordinates, an internal tidal wave appears to be a lobe. The direction of the first wave is thus determined from the biggest lobe. Thus, the amplitude A, phase ϕ, and propagation direction θ of one internal tidal wave are determined. Afterward, its signal is predicted and subtracted from the original data, which removes the wave itself and its side lobes. This procedure can

be repeated to extract an arbitrary number of waves one by one. Note that the resultant internal tidal waves are sorted with descending amplitudes.

The frequency (ω) and horizontal wavenumber (k) of the target internal tides are needed in plane wave analysis. The M_2 and N_2 tidal periods (equivalent to frequencies) are from the Moon's orbital motion around the Earth (Doodson, 1921; Pawlowicz et al., 2002). They are 12.4206 and 12.6583 hours, respectively. The local phase speed (equivalent to wavenumber) of the target internal tides is theoretically determined from the World Ocean Atlas 2018 (WOA18) (Boyer et al., 2018). The WOA18 provides climatological hydrographic profiles on a spatial grid of 0.25° latitude by 0.25° longitude. Ocean depth is based on the 1-arc-minute topography database constructed using in situ and satellite measurements (Smith and Sandwell, 1997). For given ocean depth and stratification profile, the vertical structures and eigenvalue speeds of internal tides are obtained by solving the Sturm-Liouville equation (Gill, 1982; Chelton et al., 1998)

$$\frac{d^2\Phi(z)}{dz^2} + \frac{N^2(z)}{c^2}\Phi(z) = 0, \tag{2}$$

subject to the boundary conditions $\Phi(0) = \Phi(-H) = 0$, where H is the ocean depth, and $N(z)$ is buoyancy frequency profile, and c is the eigenvalue speed. The phase speed c_p can be calculated from the eigenvalue speed following

$$c_p = \frac{\omega}{\sqrt{\omega^2 - f^2}}c, \tag{3}$$

where ω and f are the tidal and inertial frequencies, respectively. Note that the phase speed is a function of longitude and latitude (Zhao et al., 2016).

2.3 Mapping procedure

Our three-step mapping procedure consists of two rounds of plane wave analysis and a spatial two-dimensional (2D) bandpass filter in between (Zhao, 2020, 2021, 2022a, b). In this paper, the mapping process is illustrated by showing intermediate results in Figure 3. An interested reader is referred to the above papers for more details.

In step 1, mode-1 N_2 internal tides are mapped by plane wave analysis as described above. The N_2 internal tides are mapped from along-track SSH data onto a spatially regular grid. In this paper, our fitting window is chosen to be 160 km by 160 km, consistent with wavelengths of mode-1 N_2 internal tides. The resulting N_2 internal tides are at a 0.2° longitude by 0.2° latitude grid. At each grid point, five mode-1 N_2 internal tidal waves of arbitrary propagation directions are fitted. The vector sum of these five waves gives the internal tide solution. Figure 3a shows the mode-1 N_2 internal tide field obtained. It gives obvious internal tide signals (e.g., around the Hawaiian Ridge), but the nontidal noise is high. In step 2, the spatially regular N_2 internal tide field is cleaned by a 2D bandpass filter in overlapping 850 km by 850 km windows. The N_2 internal tide field is first converted to the 2D wavenumber spectrum by Fourier transform. The spectrum is truncated to [0.8 1.25] times the local wavenumber. The truncated spectrum is converted back to the internal tide field by inverse Fourier transform. Figure 3b shows the cleaned N_2 internal tide field. Now the N_2 internal tide signals are much cleaner. However, Figure 3b cannot resolve multiple internal tidal waves. In step 3, plane wave analysis is called again to decompose the filtered internal tide field into five internal waves of arbitrary propagation directions. The second-round plane wave analysis is same as the first-round plane wave
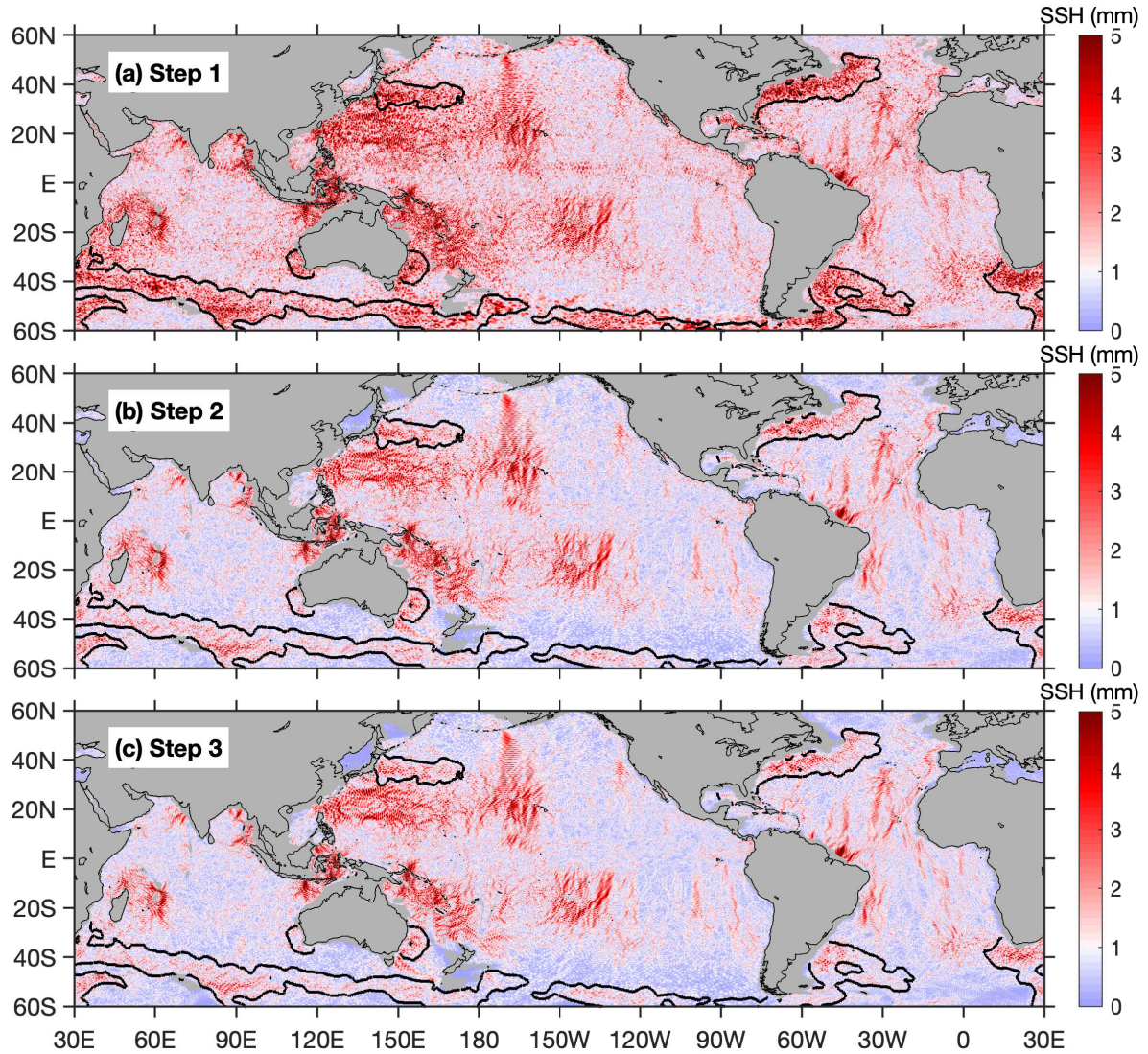
Figure 3. The 3-step mapping procedure. (a) Mode-1 N_2 internal tides obtained by the first-round plane wave analysis. (b) Mode-1 N_2 internal tides are cleaned by 2D bandpass filtering. (c) Mode-1 N_2 internal tides are decomposed by the second-round plane wave analysis. Shown here is the 5-wave superposed amplitude.

analysis, except that the input is the filtered internal tide field in step 2. In the end, the resulting five waves are saved with their respective amplitudes, phases and directions. Figure 3c shows the 5-wave superimposed internal tide field. It is very similar to Figure 3b, because this step only decompose the internal tide field. The 5-wave decomposition allows us to separate internal tides of different propagation directions. They will be used to extract long-range internal tidal beams in the ocean (Section 3).

2.4 N_2 and M_2 internal tides

We map both the mode-1 N_2 and M_2 internal tides following the same 3-step procedure. They are constructed using the same satellite altimetry data, but using their own wave parameters (frequencies and wavenumbers). Figure 4 shows the resulting N_2 and M_2 internal tide fields. Internal tides in shallow waters (<1000 m) are discarded. The new M_2 internal tides are almost identical to those obtained in previous studies using slightly different satellite data (Zhao, 2022b). In this study, we find that the N_2 and M_2 internal tides have similar spatial patterns, and that the N_2 amplitudes are about 20% of the M_2 amplitudes. The largest N_2 amplitudes are about 5 mm, compared to 20–30 mm for M_2 internal tides. To account for this factor, their colormap ranges are different by a factor of five. Figure 4 gives SWOT's ground tracks in its one-day fast-repeating phase (green lines). It shows that strong mode-1 N_2 internal tides occur under some SWOT swaths, for example, those off the California coast, in the New Caledonia region, in the western North Pacific, and on the Amazon continental shelf. In these regions, the N_2 internal tides cannot be neglected in the study of sub-mesoscale dynamics. Conversely, the new SWOT data also offer a great opportunity for us to explore internal tides.

We have examined the possible cross-talk between the N_2 and M_2 internal tides in our mapping procedure. We map N_2 internal tides using two different data sets. The first is the original satellite altimetry SSH data set (Section 2.1). The second is the M_2-corrected data set. In other words, the M_2 internal tides are predicted using our empirical model and subtracted from the original data. We find that the resulting N_2 internal tides from the two data sets are almost the same. The variance of their differences is <1% that of the N_2 internal tides. Likewise, we map M_2 internal tides using both the original and N_2-corrected data sets, respectively, and find that the impact of N_2 on M_2 is negligible. Our analysis reveals that the N_2 and M_2 internal tides do not crosstalk in our mapping method. It is because the 27-year-long satellite data from 1993 to 2019 are sufficient to unambiguously separate the N_2 and M_2 tidal constituents.

2.5 Model errors

Errors in the our N_2 and M_2 internal tide models are estimated using background internal tides. The background internal tides are mapped using the same satellite data and following the same mapping procedure, but using different wave parameters. In our mapping procedure, they are the period and wavenumber of the target internal tides. The wavelength (phase speed) is a function of tidal period, and can be determined using Equation (3). As describe above, that N_2 and M_2 internal tides are mapped using tidal periods of 12.4206 and 12.6583 hours, respectively. Here we map 13 sets of internal tides using 13 different tidal periods. Specifically, the tidal periods are linearly interpolated between M_2 and N_2 (Figure 5). We thus obtain 13 background internal tides in the central Pacific (Figure 4c, box). As expected, the SSH amplitudes of the 13 sets of internal tides are small. Figure 5 shows that their regional mean SSH amplitudes in the central Pacific are 0.8±0.1 mm, compared to 1.66 and 7.75 mm for N_2 and M_2. In addition, we calculate the correlation coefficients among these 15 sets of internal tides. All of the correlation coefficients are <0.05, suggesting that these background internal tides are independent with each other and with the N_2 and M_2 internal tides. Thus, we suggest that the model errors in N_2 and M_2 can be indicated by the background internal tides. In other words, the background internal tides are the signals we obtain where there are no tidal constituents at all. In this study,
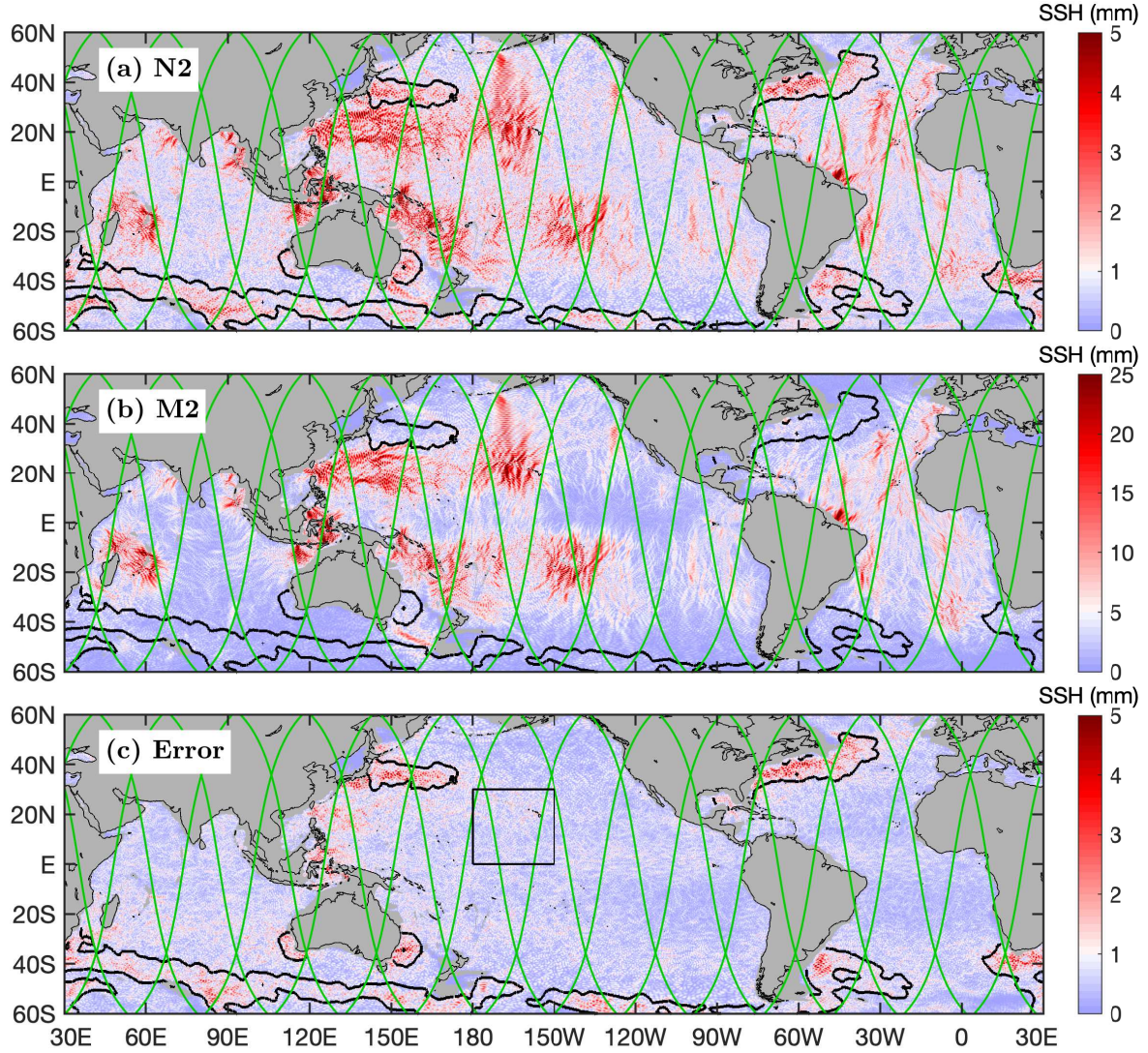
Figure 4. Internal tides and model errors. Shown are their SSH amplitudes. (a) N_2. (b) M_2. (c) Errors. The model errors are estimated using a background tidal period (12.6074 hours) using the same satellite altimetry data. N_2 and M_2 have similar spatial patterns. The N_2 amplitudes are about 20% of the M_2 amplitudes. Black contours indicate regions of strong currents, where both models have large model errors. Green lines denote SWOT ground tracks in the fast-repeating phase. The mean SSH amplitude in the black box is given in Figure 5
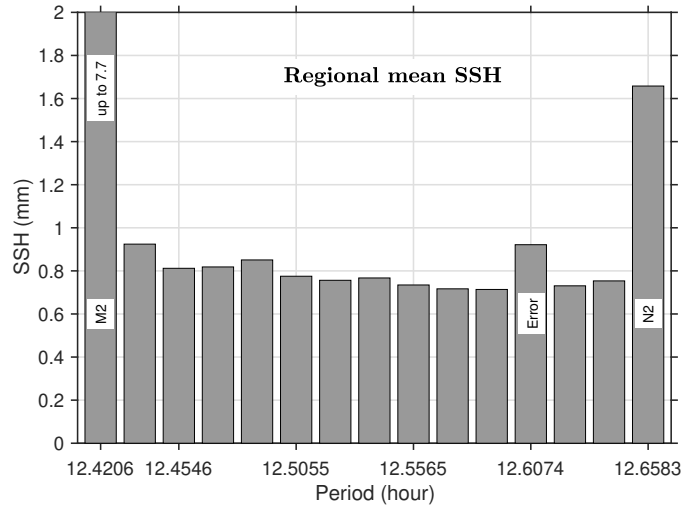
Figure 5. Histogram of regional mean SSH amplitudes. In the central Pacific Ocean ($0°$–$30°$N, $180°$–$150°$W), 15 sets of internal tides are determined using the same satellite data and following the same procedure. They are mapped using their respective periods and wavenumbers. Tidal periods of the 13 sets of background internal tides are linearly interpolated between M_2 and N_2.

we choose a tidal period of 12.6074 hours to construct a global map of internal tides (because a global run is time consuming), which is taken as model errors. Figure 4c gives the global map of model errors. It reveals that the model errors are large in regions of strong currents (black contours). Figure 4 shows that the N_2 internal tides are noisier than M_2, because their small SSH amplitudes are easily affected by the same model errors.

2.6 Model evaluation

Our N_2 internal tide model is evaluated using independent satellite SSH data collected in 2020 and 2021. For each SSH measurement of known time and location, the internal tide signal is predicted using the model under evaluation, and subtracted from the SSH measurement. Variance reduction is the variance difference before and after the internal tide correction. The variance reductions for all SSH measurements are binned into $2°$ by $2°$ boxes. The global map of variance reduction is shown in Figure 6a. In regions of strong currents (black contours), the N_2 internal tides have large errors. The M_2 internal tide model is evaluated in the same way and shown in Figures 6b. Note that the colormap ranges for N_2 and M_2 are different by a factor of 25, the square of the factor in their amplitudes.

In the evaluation, the true N_2 internal tides in the model (variance σ_{N2}) will remove the N_2 internal tides in the independent data, leading to positive variance reduction. While the model errors (variance σ_ϵ) will increase the variance of the independent data, leading to negative variance reduction. Together, one obtains positive variance reduction where $\sigma_{N2} > \sigma_\epsilon$, and negative variance reduction where $\sigma_{N2} < \sigma_\epsilon$. Figure 6a shows that the global ocean is dominated by positive variance reduction, suggesting that the true N_2 internal tides are usually greater than model errors. In particular, in regions of strong N_2 internal tides such as the Hawaiian Ridge and the Amazon continental shelf, patches of positive variance reduction are observed, because

the strong N_2 internal tides can overcome model errors. For the same reason, negative variance reduction usually occurs in regions of weak N_2 internal tides such as the eastern equatorial Pacific and the Southern Ocean. The regions of strong currents (black contours) are dominated by negative variance reduction, where weak N_2 internal tides are overwhelmed by model errors (Figure 4c).

For comparison, Figure 6b shows that the M_2 internal tide model causes positive variance reduction throughout the global ocean, except for regions of strong currents (black contours) and some regions with strong time variability (Zhao, 2021). It is because the strong M_2 internal tides (five times N_2) are dominantly greater than the same model errors $\sigma_{M2} > \sigma_{\epsilon}$. In summary, our empirical N_2 internal tide model can reduce variance in most ocean regions, although the N_2 amplitudes are just a few mm. Figure 6 shows that, in its fast-repeating phase, the SWOT swaths cover some regions of strong N_2 and M_2 internal tides (off the California coast, the Amazon continental shelf, the western North Pacific, and the New Caledonia). In these regions, we clearly see positive variance reduction, which means that our N_2 and M_2 internal tide models can make internal tide correction for SWOT.

3 Results

3.1 Global distribution

Our new N_2 model reveals that mode-1 N_2 internal tides are widespread in the global ocean (Figure 4a). In the Indian Ocean, they are observed in the Arabian Sea, the Bay of Bengal, and the Madagascar-Mascarene region. In the Pacific Ocean, N_2 internal tides occur in regions such as the French Polynesian Ridge, the Hawaiian Ridge, the Indonesian seas, the western South Pacific, and the western North Pacific. In the Atlantic Ocean, N_2 internal tides appear in regions including the Azores region, the Amazon shelf, the Bay of Biscay, and the Vitoria-Trindade Ridge. Our M_2 model reveals that mode-1 M_2 internal tides are observed in the same regions (Figure 4b). The N_2 and M_2 internal tides have similar spatial patterns, but the N_2 amplitudes are about 20% of the M_2 amplitudes. To further quantify their relation, we give in Figure 7a the scatter plot of the N_2 and M_2 SSH amplitudes. It shows that the N_2 and M_2 amplitudes largely follow the diagonal line with a ratio of 5. Their correlation coefficient is 0.69 (R in Matlab function *corrcoef*).

We extract the N_2 and M_2 barotropic tides from TPXO.8 (Egbert and Erofeeva, 2002), and show them in Figures 8. We find that the N_2 and M_2 barotropic tides have similar spatial patterns, and that the N_2 amplitudes are about 20% of the M_2 amplitudes. We examine the relation between the N_2 and M_2 barotropic tides as well. Figure 7b shows the scatter plot of the N_2 and M_2 barotropic amplitudes. It shows that N_2 and M_2 have a very tight relation, with their correlation coefficient being 0.96. Egbert and Ray (2003) show that the M_2 and N_2 barotropic-to-baroclinic energy conversion maps have similar spatial patterns, and that their amplitudes differ by a factor of 25 (see their Figure 1). The N_2 and M_2 relation (spatial pattern and amplitude ratio) is the same for both barotropic and baroclinic tides. Because N_2 and M_2 have close tidal periods (12.6583 and 12.4206 hours), their generations over the same topographic features should be the same. In addition, it is reasonable that the N_2 and M_2 internal tides have a relatively weak relation (Figure 4a), because the long-range propagation of internal tides is affected by an inhomogeneous ocean environment.
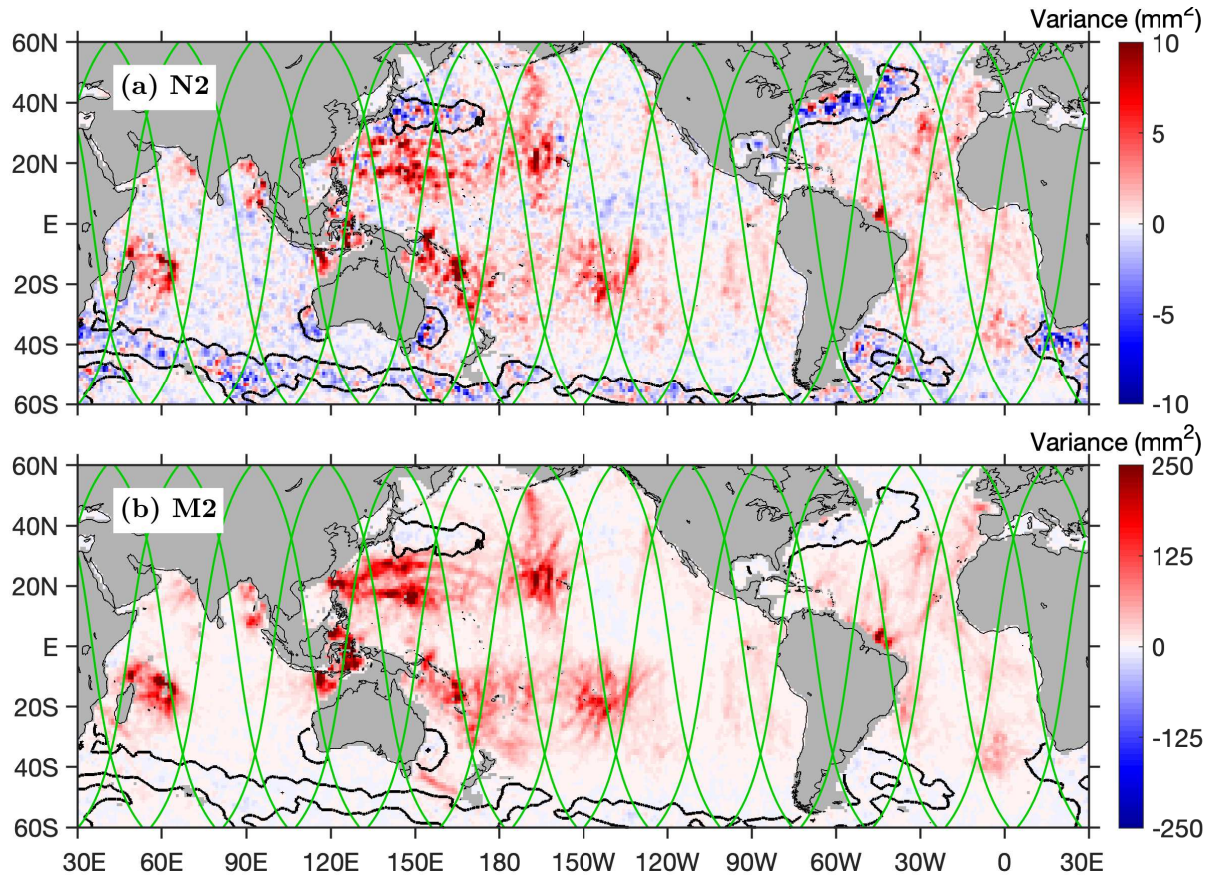
Figure 6. Model evaluation. Both internal tide models are evaluated using independent satellite altimetry data in 2020 and 2021. Shown are their variance reduction binned in $2°$ by $2°$ boxes. The black contours indicate regions of strong currents, where both the N_2 and M_2 models have larger errors and negative variance reductions. Green lines denote SWOT ground tracks in the fast-repeating phase.

3.2 Long-range beams

In this section, we study the long-range mode-1 N_2 internal tidal beams. We have fitted five mode-1 N_2 internal tidal waves at each grid point by plane wave analysis. Taking advantage of the 5-wave fits, we can decompose the N_2 internal tide field into the northward ($0°$–$180°$ anti-clockwise from due east) and southward ($180°$–$360°$) components by propagation direction. Each

215 component contains internal tidal waves with propagation directions falling in the given range (Figure 9). The decomposed components clearly show well-defined long-range N_2 internal tidal beams, which are characterized by larger amplitudes and cross-beam co-phase lines (no shown here for clarity). There are numerous long-range N_2 internal tidal beams, which radiate from the strong generation sites mentioned above. For example, northward N_2 beams are observed to originate from the French Polynesian Ridge, the Macquarie Ridge, the Amazon shelf, and so on. Southward N_2 beams are observed to originate from

220 the Andaman Islands, the Lombok Strait, the Hawaiian Ridge, the French Polynesian Ridge, the Mendocino Ridge, the Azores
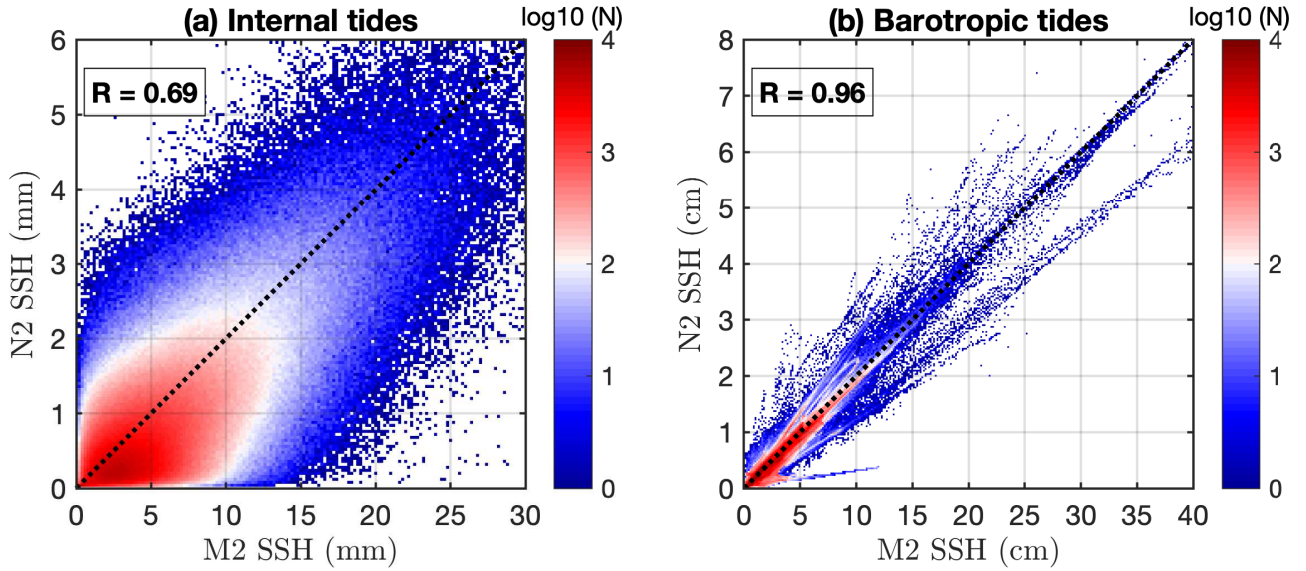
Figure 7. Relations between N_2 and M_2 amplitudes. (a) Internal tides. (b) Barotropic tides. Shown is data density in logarithmic scale. Their correlation coefficients (R) are calculated. For both the barotropic and internal tides, the N_2 amplitudes are about 20% of the M_2 amplitudes.

Islands, among others. Note that the M_2 long-range internal tidal beams have been well studied in previous studies (Zhao et al., 2016, Figure 5 therein). To avoid repetition, the M_2 internal tidal beams are not shown here. From our new results, we observe that the N_2 and M_2 internal tides have similar long-range beams. Our new N_2 and M_2 internal tide models are freely available (see *data availability*). In this study, we examine two long-range internal tidal beams as examples.

225   First, we examine the southward internal tides from the Amukta Pass, Alaska. The M_2 long-range beam from Amukta Pass has been studied recently (Zhao, 2022b). Figure 10a shows the southward N_2 internal tides in the central North Pacific (Figure 9b, box). For comparison, the southward M_2 internal tides are shown in Figure 10b. Both tidal constituents can travel from the Aleutian island chain to the Hawaiian Ridge over 3,000 km away. Their propagation directions are about $-78°$ from due east. The black lines shows the $0°$ and $180°$ co-phase charts. Figure 10c shows their phase difference, which increases with propagation, because N_2 internal tides travel faster than M_2 internal tides according to Equation (3). In the propagation, their phase difference increases with propagation. Along the dashed line from source (52.6°N, 189°E) to far field (26°N, 195°E), their phase difference increases from $65°$ to $305°$. The overall phase change is $240°$. Note that the length of the dashed line is 3000 km. It takes about 18 tidal cycles for the N_2 or M_2 internal tides to travel along the line.

Figure 11 shows southward internals tides in the region off the California Coast. This region is chosen for a detailed in-235   vestigation, because it contains one site for the SWOT calibration/validation field experiment. The green lines in this figure indicate SWOT swaths in the fast-repeating phase (Wang et al., 2022). The cross-over region of the ascending and descending swaths is the SWOT calibration/validation site. This region is dominated by the southward internal tides from the Mendocino Ridge. Note that this region is also affected by internal tides in other propagation directions (not shown). Additionally, there are
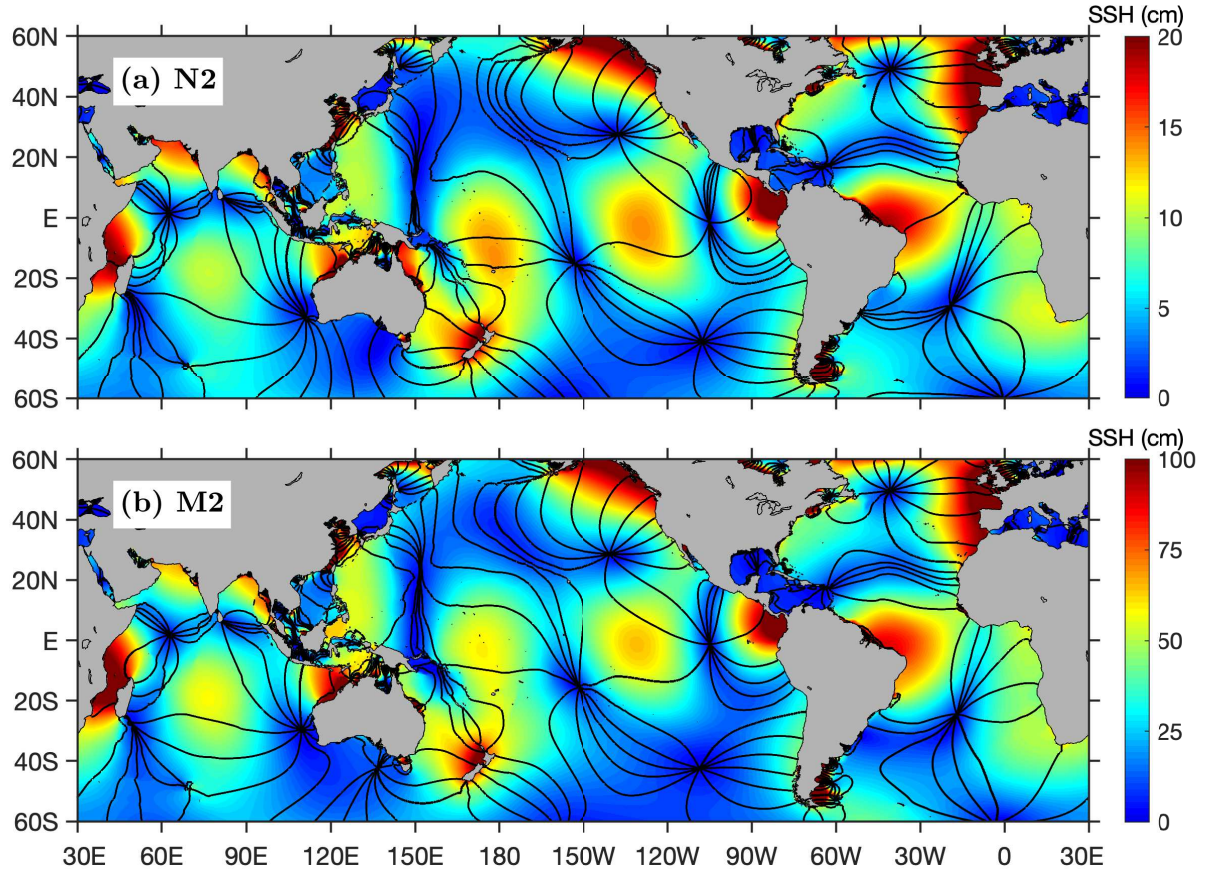
Figure 8. N_2 and M_2 barotropic tides from TPXO.8 (Egbert and Erofeeva, 2002). Colors show amplitude. Black lines show co-phase charts at 30° intervals. N_2 and M_2 have similar spatial patterns, and the N_2 amplitudes are about 20% of the M_2 amplitudes.

southwestward internal tides from the Monterey Bay. The two internal tidal beams intersect around the SWOT experiment site. As explained earlier, our N_2 internal tide model is available for SWOT correction. The results shows that N_2 and M_2 internal tides are very similar, although the N_2 fluxes are much weaker. Both N_2 and M_2 beams can be tracked from about 40°N to 20°N over 2000 km. They both bifurcate around 32°N near Fieberling Seamounts (32.5°N, 232.3°E). The dashed line labels the beam from 40.3°N to 22°N along 128°W. This line is about 2000 km long. Along this line, the N_2 and M_2 phase difference increases from 40° to 160°, that is,120° over about 14 M_2 or N_2 tidal cycles.

3.3 Energy flux

We calculate the depth-integrated energy flux of mode-1 N_2 internal tide from their SSH amplitudes and a transfer function (F_n). The transfer function is calculated using the WOA18 climatological hydrography and the Sturm-Liouville equation (Zhao and Alford, 2009; Zhao et al., 2016). Our calculation method is confirmed by Geoffroy and Nycander (2022). In this study,
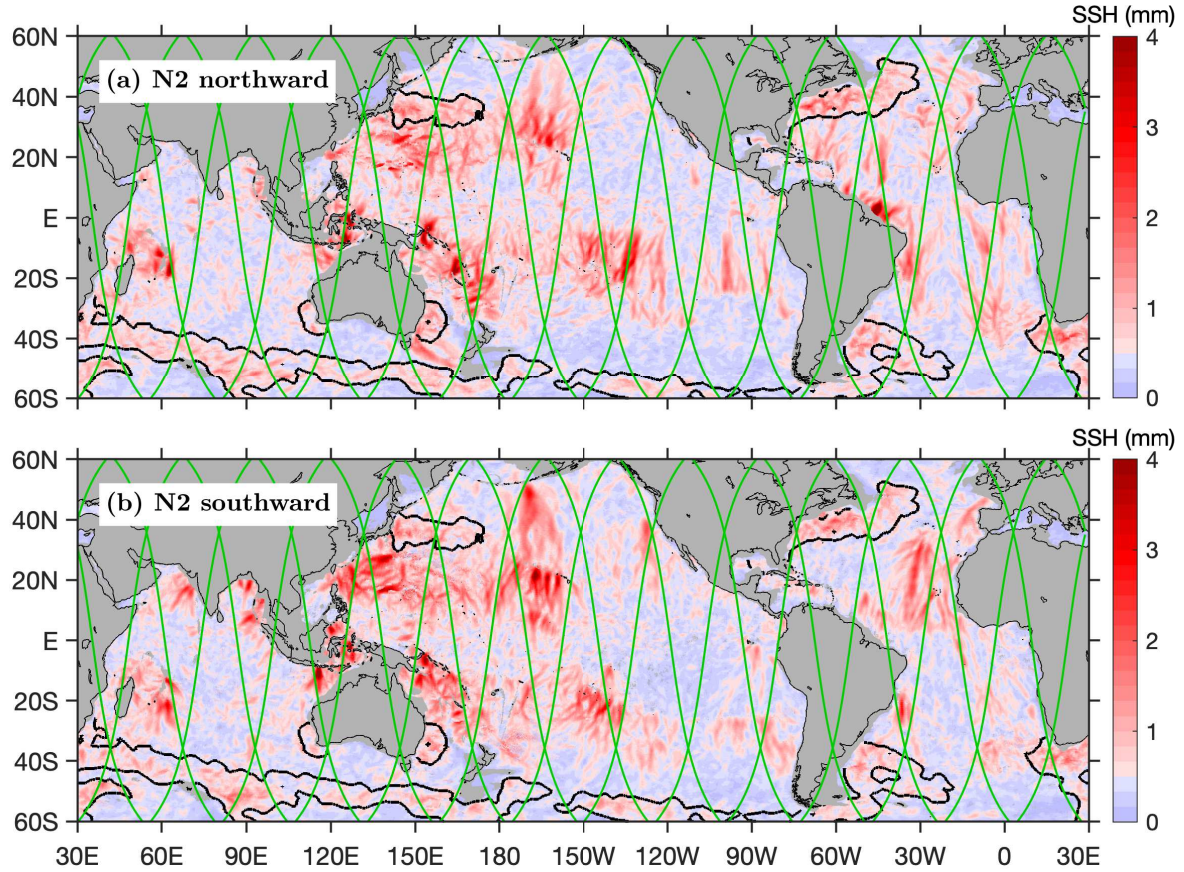
Figure 9. Two decomposed N_2 internal tide fields. (a) Northward component (directional range: $0°$–$180°$ anti-clockwise from due east). (b) Southward component (directional range: $180°$–$360°$). Internal tides in shallow waters (<1000 m) are discarded. Black contours indicate regions of strong currents, where both the N_2 and M_2 models have larger errors. Green lines denote SWOT ground tracks in the fast-repeating phase.

we repeat our method (previously for mode-1 M_2 internal tides) to obtain the transfer function for mode-1 N_2 internal tides. It
250 is a function of ocean depth, tidal frequency, mode number, latitude, and stratification. The transfer functions for N_2 and M_2 are very close, because their tidal periods are close. At each grid point, we thus obtain five energy fluxes for the five internal tidal waves following $F = \frac{1}{2} F_n A^2$, where A is the SSH amplitude. The vector sum of the five energy fluxes gives the final energy flux at this site. In this study, we compare the N_2 and M_2 internal tide energy fluxes in two regions. Our model results are freely available (see *data availability*). An interested reader can examine other ocean regions. We show that their energy
255 fluxes have similar spatial patterns, but their flux magnitudes have a ratio of 1/25 (i.e., the square of their amplitude ratio). The results show that the mode-1 N_2 internal tides can be observed by satellite altimetry, although their are much weaker than the M_2 internal tides.
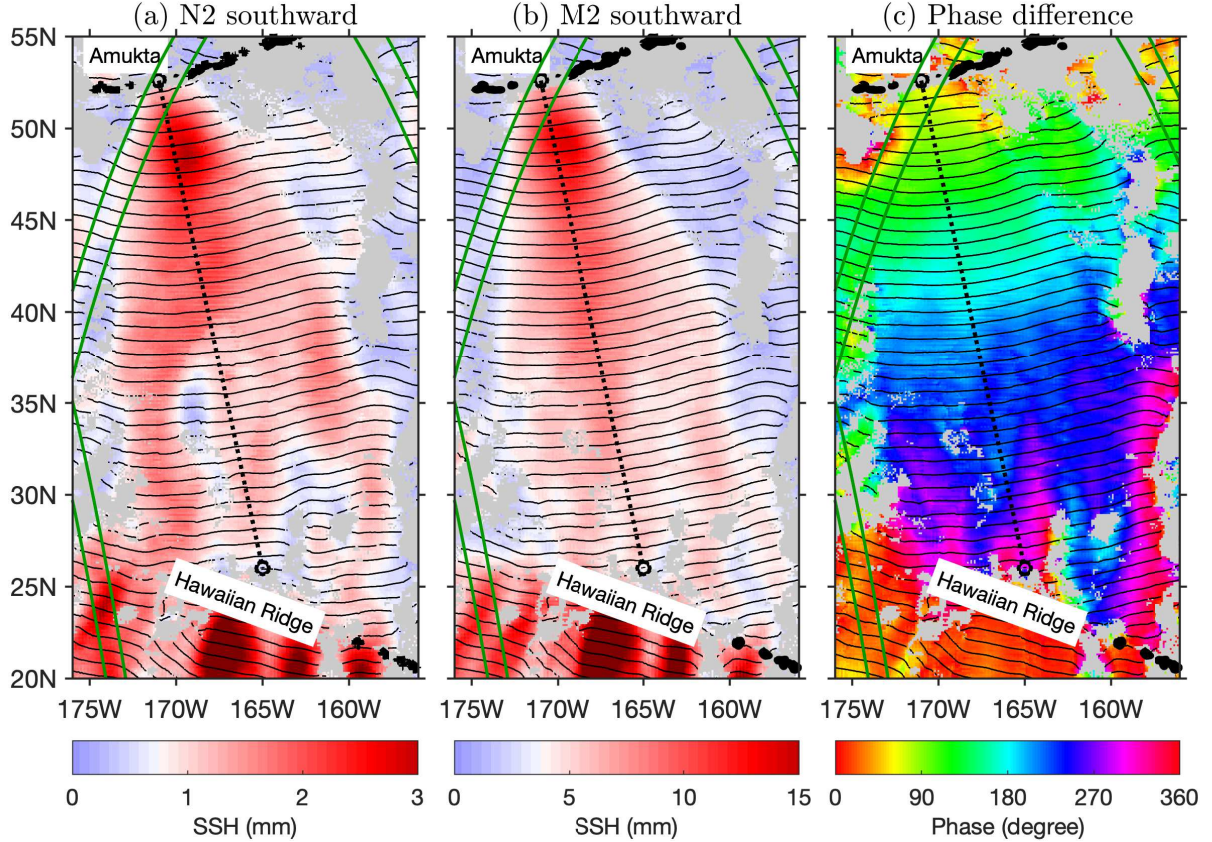
Figure 10. Southward internal tides from Amukta Pass, Alaska ($180°$–$360°$). (a) N_2 internal tides. (b) M_2 internal tides. Black contours show the $0°$ and $180°$ co-phase charts. Intervals between two neighboring co-phase lines are half wavelengths. (c) Phase difference between N_2 and M_2. Black contours show the M_2 co-phase chart as in (b). Weak internal tides are discarded (M_2 <1 mm; N_2 <0.2 mm). Both N_2 and M_2 internal tides can propagate over 3000 km from the Aleutian Ridge to the Hawaiian Ridge. Along the 3000-km-long dashed line, the phase difference increases from $60°$ to $300°$. Green lines denote the 120-km-wide SWOT swaths in the fast-repeating phase.
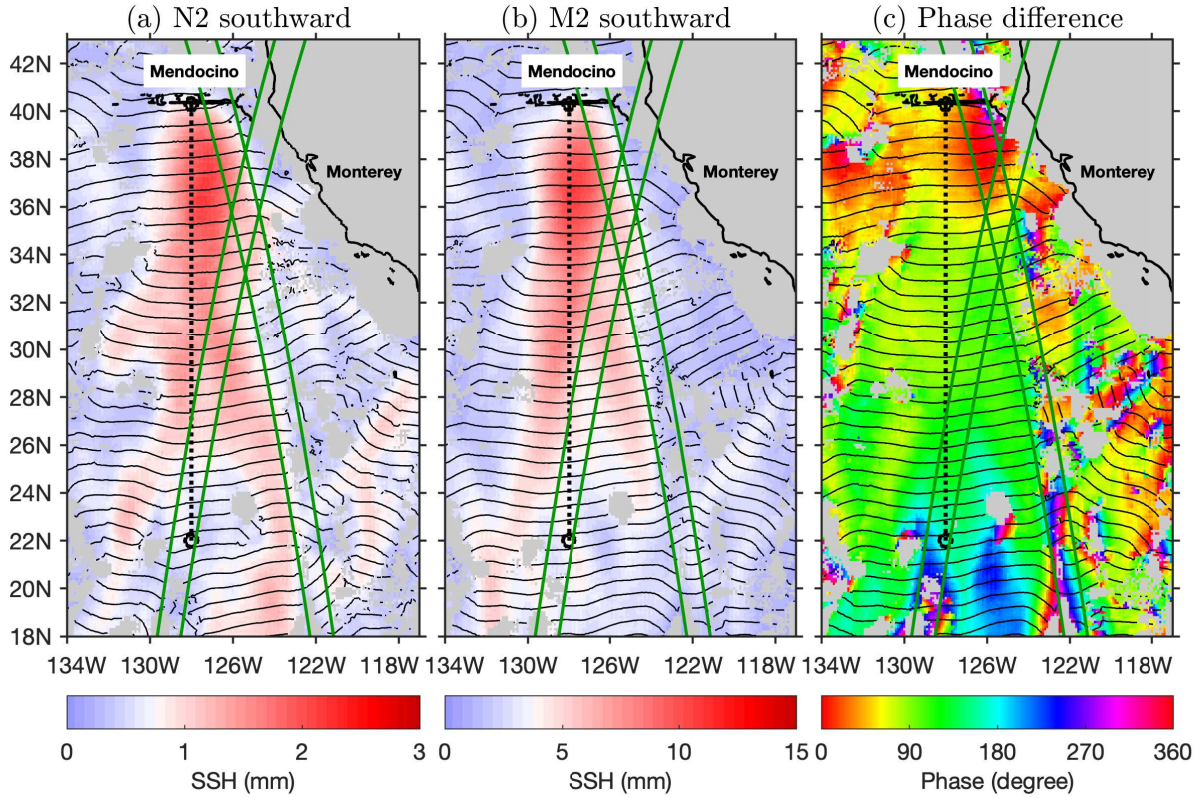
Figure 11. Southward internal tides off the U.S. West Coast ($180°$–$360°$). (a) N_2. (b) M_2. Colors show SSH amplitudes. Black contours indicate the $0°$ and $180°$ co-phase charts. Southward internal tides are mainly radiate from the Mendocino Ridge. Weak internal tides are discarded (M_2 <1 mm; N_2 <0.2 mm). Internal tides in shallow waters (<1000 m) are discarded. Green lines denote two 120-km-wide SWOT swaths in the fast-repeating phase.

Figure 12 shows the N_2 and M_2 energy fluxes in the western South Pacific. In this study, it is trimmed to $30°$S–$0°$, $145°$E–$135°$W. Colors show flux magnitudes, and black arrows show flux vectors. This region is chosen because (1) it features various topographic obstacles such as mid-ocean ridge and island chain, and (2) the New Caledonia region is one site for SWOT calibration/validation (Bendinger et al., 2023). There are numerous N_2 and M_2 internal tidal beams in this region. They are dominantly generated over topographic features. For example, N_2 and M_2 internal tidal beams radiate from many straits in the Coral Sea (Tchilibou et al., 2020). The internal tidal beams can be in any horizontal propagation direction. From the French Polynesian Ridge, internal tides mainly propagate southward and northward. From the Kermadec Arc and the New Caledonia, the outgoing internal tidal beam usually travel eastward or westward. The energy fluxes of N_2 and M_2 internal tides have similar spatial patterns. Their flux magnitudes are different by a ratio of 25, which can be inferred from their SSH amplitudes. Figure 12 shows seven SWOT swaths in this region (green lines). Among the, the two swaths in the New Caledonia region
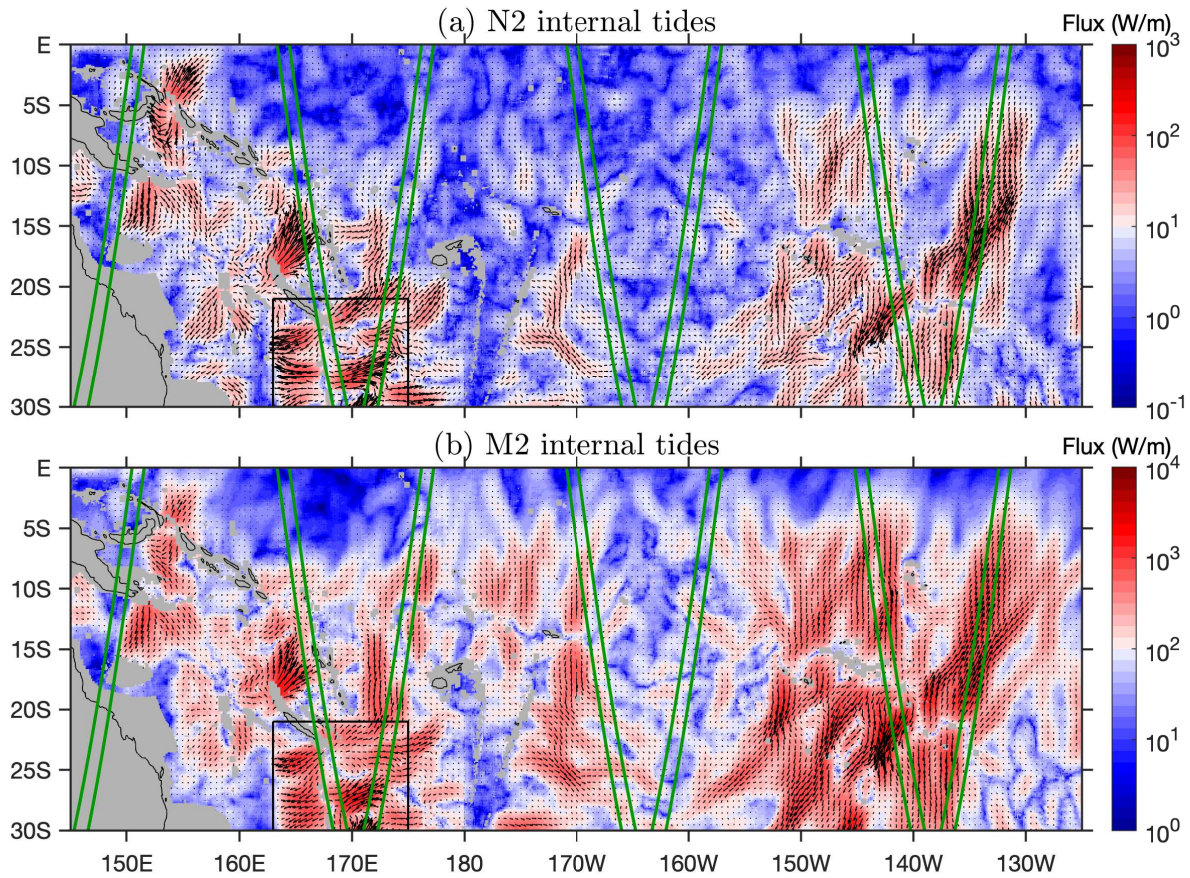
Figure 12. Internal tide energy flux in the western South Pacific. (a) N_2 internal tides. (b) M_2 internal tides. Colors show flux magnitudes, and black arrows show flux vectors. Internal tides in shallow waters (<1000 m) or in regions of strong currents are discarded (gray shading). Green lines indicate SWOT swaths in the fast-repeating phase.

(black box) overlap with strong N_2 internal tides. In addition, the two swaths lie cross the French Polynesian Ridge. One should pay an attention to N_2 and M_2 internal tides in the study of mesoscale and sub-mesoscale processes.

Figure 13 shows the N_2 and M_2 energy fluxes in the North Atlantic Ocean (2°S–53°N, 58°W–3°W). Figure 13 is in the same format as Figure 12. Internal tides in this region have attracted much attention in recent years (Vic et al., 2018; Köhler et al., 2019; Löb et al., 2020). In particular, internal tides on the Amazon shelf have been intensively studied recently, partly because of the co-existence of internal tides and internal solitary waves (Egbert and Erofeeva, 2021; Tchilibou et al., 2022; Assene et al., 2023). Our satellite observation reveals that N_2 and M_2 internal tide fields occur around notable topographic features including the Mid-Atlantic Ridge, the Amazon shelf, the Azores region (black box), the Bay of Biscay, Canary Islands, and the Cape Verde islands. The longest internal tidal beams for both N_2 and M_2 are the southward internal tidal beams from the
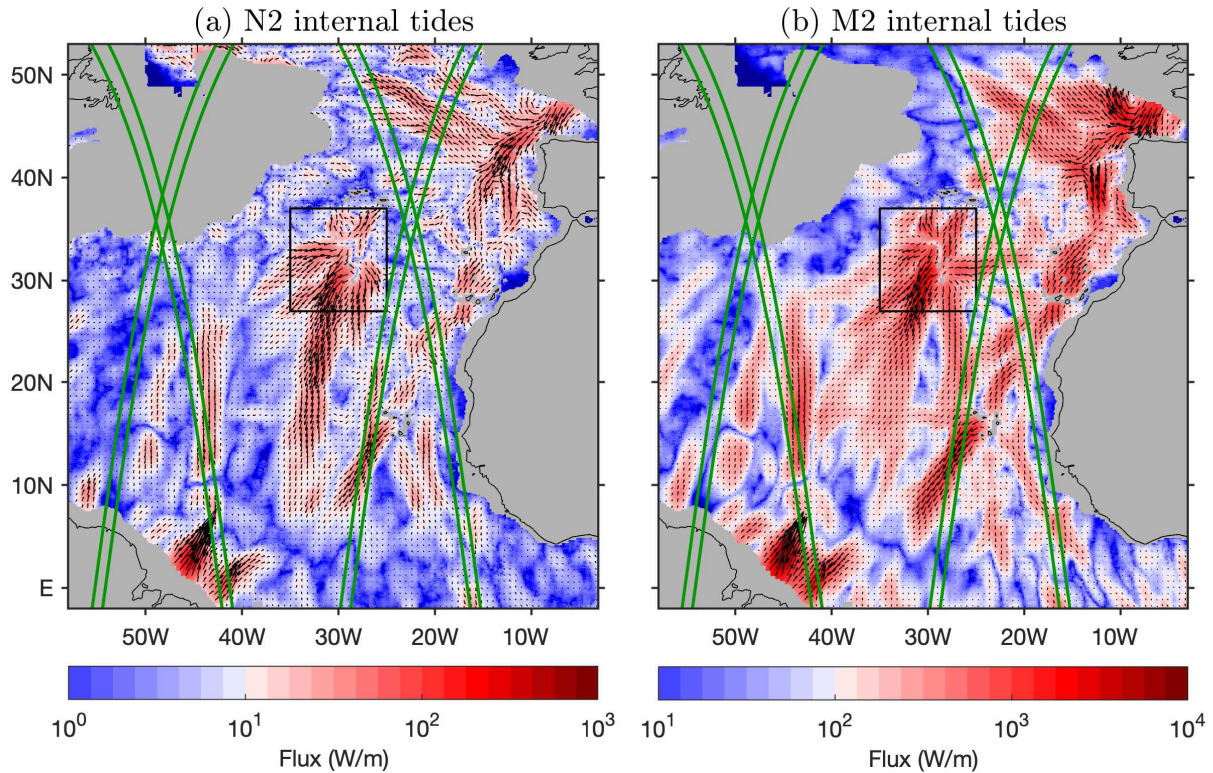
Figure 13. As in Figure 12 but for internal tide energy flux in the North Atlantic Ocean.

Azores (Zhao, 2016; Köhler et al., 2019). The two beams can be tracked over 2000 km. In this region, there are four SWOT swaths (in its fast-repeating phase), which meet some remarkable N_2 and M_2 internal tidal beams.

4   Summary

280   In this study, we have constructed an empirical mode-1 N_2 internal tide model from satellite altimetry. N_2 is the larger lunar elliptical semidiurnal constituent and the fifth largest oceanic tidal constituent. It is induced by the Moon's elliptical orbit. Its amplitudes are about 20% of the M_2 amplitudes. The mode-1 N_2 internal tides have sub-centimeter-scale SSH amplitudes. We can observe the weak mode-1 N_2 internal tides, because we use a larger satellite altimetry data set and a new mapping procedure. First, we use the multiyear multisatellite altimetry data from 1993 to 2019. The combined data are about

285   100 satellite-years long, which can significantly suppress nontidal errors. Second, we extract mode-1 N_2 internal tides by a newly-developed mapping procedure. This procedure cleans the internal tide field using the known frequency and theoretical wavenumber of the target internal tide. In consequence, satellite altimetry can observe mode-1 N_2 internal tides with mm-scale SSH amplitudes. Our mode-1 N_2 internal tide model is still noisy. Future improvements can be made with more and more satellite altimetry data becoming available.

Our newly-developed N_2 internal tide model is evaluated using independent satellite altimetry data in 2020 and 2021. It shows that the empirical model can significantly remove N_2 internal tides, and cause positive variance reduction in most ocean regions, in particular, in source regions over topographic features. Therefore, the N_2 internal tide model can make internal tide correction for SWOT. Our N_2 model reveals the basic features of the global N_2 internal tides. We find that N_2 and M_2 internal tides have similar spatial patterns, and that the N_2 amplitudes are about 20% of the M_2 amplitudes. Both features stem from their barotropic counterparts. We also find that N_2 and M_2 have similar spatial patterns in terms of barotropic tide and barotropic-to-baroclinic energy conversion. We observe that both N_2 and M_2 internal tides can propagate hundreds to thousands of kilometers in the open ocean, but at different phase speeds. Including N_2 internal tides can better describe the temporal variation of internal tide-driven ocean mixing with the lunar elliptical orbit cycle (27.5546 days).

Last but not least, we demonstrate in this study that our mapping technique can construct a reliable mode-1 N_2 internal tide model using 100 satellite-years altimetry data. We estimate that our model errors are usually <1 mm in the global ocean (Figure 4c). We have applied our mapping technique to other minor tidal constituents and higher baroclinic modes (modes 2–4), and obtained promising signals. We will continue to map other minor tidal constituents and higher baroclinic modes. It is expected that the low-noise SWOT data along 120-km-wide swaths will greatly improve the observation of minor tidal constituents. When the SWOT data are available, we will surely analyze the SWOT data by our technique.

Data availability. The satellite altimetry along-track data are from the Copernicus Marine Service (https://doi.org/10.48670/moi-00146). The satellite altimetry gridded data are from the Copernicus Marine Service (https://doi.org/10.48670/moi-00148). The SWOT orbit data are from the AVISO website (https://www.aviso.altimetry.fr/en/missions/current-missions/swot). The World Ocean Atlas 2018 is produced and made available by NOAA National Oceanographic Data Center (https://www.nodc.noaa.gov/OC5/woa18/). The M_2 and N_2 internal tide models developed in this study are made free available to the public when this manuscript is accepted.

Author contributions. This paper is completed by the sole author.

Competing interests. The author has declared there are no competing interests.

Acknowledgements. This study was funded by the National Aeronautics and Space Administration (NASA) via projects NNX17AH57G and 80NSSC18K0771.

References

Arbic, B. K.: Incorporating tides and internal gravity waves within global ocean general circulation models: A review, Progress in Oceanography, 206, 102 824, https://doi.org/10.1016/j.pocean.2022.102824, 2022.

Assene, F., Koch-Larrouy, A., Dadou, I., Tchilibou, M., Morvan, G., Chanut, J., Vantrepotte, V., Allain, D., and Tran, T.-K.: Internal tides off the Amazon shelf Part I : importance for the structuring of ocean temperature during two contrasted seasons, EGUsphere, 2023, 1–46, https://doi.org/10.5194/egusphere-2023-418, 2023.

Bendinger, A., Cravatte, S., Gourdeau, L., Brodeau, L., Albert, A., Tchilibou, M., Lyard, F., and Vic, C.: Regional modeling of internal tide dynamics around New Caledonia: energetics and sea surface height signature, EGUsphere, 2023, 1–53, https://doi.org/10.5194/egusphere-2023-361, 2023.

Boyer, T. P., García, H. E., Locarnini, R. A., Zweng, M. M., Mishonov, A. V., Reagan, J. R., Weathers, K. A., Baranova, O. K., Paver, C. R., Seidov, D., and Smolyar, I. V.: World Ocean Atlas 2018, Tech. rep., NOAA National Centers for Environmental Information, https://www.ncei.noaa.gov/archive/accession/NCEI-WOA18, 2018.

Byun, D.-S. and Hart, D. E.: A monthly tidal envelope classification for semidiurnal regimes in terms of the relative proportions of the S_2, N_2, and M_2 constituents, Ocean Science, 16, 965–977, https://doi.org/10.5194/os-16-965-2020, 2020.

Chelton, D. B., deSzoeke, R. A., Schlax, M. G., El Naggar, K., and Siwertz, N.: Geographical variability of the first baroclinic Rossby radius of deformation, Journal of Physical Oceanography, 28, 433–460, https://doi.org/10.1175/1520-0485(1998)028<0433:GVOTFB>2.0.CO;2, 1998.

de Lavergne, C., Vic, C., Madec, G., Roquet, F., Waterhouse, A. F., Whalen, C. B., Cuypers, Y., Bouruet-Aubertot, P., Ferron, B., and Hibiya, T.: A Parameterization of Local and Remote Tidal Mixing, Journal of Advances in Modeling Earth Systems, 12, e2020MS002 065, https://doi.org/10.1029/2020MS002065, 2020.

Doodson, A. T.: The harmonic development of the tide-generating potential, Proceedings of the Royal Society A, 100, 305–329, https://doi.org/10.1098/rspa.1921.0088, 1921.

Dushaw, B. D.: An empirical model for mode-1 internal tides derived from satellite altimetry: Computing accurate tidal predictions at arbitrary points over the world oceans, Tech. rep., Applied Physics Laboratory, University of Washington, 2015.

Dushaw, B. D., Howe, B. M., Cornuelle, B. D., Worcester, P. F., and Luther, D. S.: Barotropic and Baroclinic Tides in the Central North Pacific Ocean Determined from Long-Range Reciprocal Acoustic Transmissions, Journal of Physical Oceanography, 25, 631–647, 1995.

Egbert, G. D. and Erofeeva, S. Y.: Efficient inverse modeling of barotropic ocean tides, Journal of Atmospheric and Oceanic Technology, 19, 183–204, 2002.

Egbert, G. D. and Erofeeva, S. Y.: An Approach to Empirical Mapping of Incoherent Internal Tides With Altimetry Data, Geophysical Research Letters, 48, e2021GL095 863, https://doi.org/10.1029/2021GL095863, 2021.

Egbert, G. D. and Ray, R. D.: Significant dissipation of tidal energy in the deep ocean inferred from satellite altimeter data, Nature, 405, 775–778, https://doi.org/10.1038/35015531, 2000.

Egbert, G. D. and Ray, R. D.: Semi-diurnal and diurnal tidal dissipation from TOPEX/Poseidon altimetry, Geophysical Research Letters, 30, 1907, https://doi.org/10.1029/2003GL017676, 2003.

Fu, L.-L. and Ubelmann, C.: On the Transition from Profile Altimeter to Swath Altimeter for Observing Global Ocean Surface Topography, Journal of Atmospheric and Oceanic Technology, 31, 560–568, https://doi.org/10.1175/JTECH-D-13-00109.1, 2014.

350 Geoffroy, G. and Nycander, J.: Global Mapping of the Nonstationary Semidiurnal Internal Tide Using Argo Data, Journal of Geophysical Research: Oceans, 127, e2021JC018 283, https://doi.org/10.1029/2021JC018283, 2022.

Gill, A. E.: Atmosphere-Ocean Dynamics, Academic Press, 1982.

Jayne, S. R. and St. Laurent, L. C.: Parameterizing tidal dissipation over rough topography, Geophysical Research Letters, 28, 811–814, https://doi.org/10.1029/2000GL012044, 2001.

355 Kelly, S. M., Waterhouse, A. F., and Savage, A. C.: Global Dynamics of the Stationary M_2 Mode-1 Internal Tide, Geophysical Research Letters, 48, e2020GL091 692, https://doi.org/10.1029/2020GL091692, 2021.

Köhler, J., Walter, M., Mertens, C., Stiehler, J., Li, Z., Zhao, Z., von Storch, J.-S., and Rhein, M.: Energy Flux Observations in an Internal Tide Beam in the Eastern North Atlantic, Journal of Geophysical Research: Oceans, 124, 5747–5764, https://doi.org/10.1029/2019JC015156, 2019.

360 Löb, J., Köhler, J., Mertens, C., Walter, M., Li, Z., von Storch, J.-S., Zhao, Z., and Rhein, M.: Observations of the Low-Mode Internal Tide and Its Interaction With Mesoscale Flow South of the Azores, Journal of Geophysical Research: Oceans, 125, e2019JC015 879, https://doi.org/10.1029/2019JC015879, 2020.

MacKinnon, J. A., Zhao, Z., Whalen, C. B., Waterhouse, A. F., Trossman, D. S., Sun, O. M., Laurent, L. C. S., Simmons, H. L., Polzin, K., Pinkel, R., Pickering, A., Norton, N. J., Nash, J. D., Musgrave, R., Merchant, L. M., Melet, A. V., Mater, B., Legg, S., Large, W. G.,

365 Kunze, E., Klymak, J. M., Jochum, M., Jayne, S. R., Hallberg, R. W., Griffies, S. M., Diggs, S., Danabasoglu, G., Chassignet, E. P., Buijsman, M. C., Bryan, F. O., Briegleb, B. P., Barna, A., Arbic, B. K., Ansong, J. K., and Alford, M. H.: Climate Process Team on Internal Wave-Driven Ocean Mixing, Bull. Amer. Meteor. Soc., 98, 2429–2454, https://doi.org/10.1175/BAMS-D-16-0030.1, 2017.

Melet, A., Legg, S., and Hallberg, R.: Climatic Impacts of Parameterized Local and Remote Tidal Mixing, J. Climate, 29, 3473–3500, https://doi.org/10.1175/JCLI-D-15-0153.1, 2016.

370 Morrow, R., Fu, L.-L., Ardhuin, F., Benkiran, M., Chapron, B., Cosme, E., d'Ovidio, F., Farrar, J. T., Gille, S. T., Lapeyre, G., Le Traon, P.-Y., Pascual, A., Ponte, A., Qiu, B., Rascle, N., Ubelmann, C., Wang, J., and Zaron, E. D.: Global Observations of Fine-Scale Ocean Surface Topography With the Surface Water and Ocean Topography (SWOT) Mission, Frontiers in Marine Science, 6, https://doi.org/10.3389/fmars.2019.00232, 2019.

Munk, W. H. and Wunsch, C.: Abyssal recipes II: Energetics of tidal and wind mixing, Deep-Sea Res. I, 45, 1977–2010,
375 https://doi.org/10.1016/S0967-0637(98)00070-3, 1998.

Pawlowicz, R., Beardsley, B., and Lentz, S.: Classical tidal harmonic analysis including error estimates in MATLAB using T_TIDE, Computers and Geosciences, 28, 929–937, 2002.

Pollmann, F., Nycander, J., Eden, C., and Olbers, D.: Resolving the horizontal direction of internal tide generation, Journal of Fluid Mechanics, 864, 381–407, https://doi.org/10.1017/jfm.2019.9, 2019.

380 Pujol, M.-I., Faugère, Y., Taburet, G., Dupuy, S., Pelloquin, C., Ablain, M., and Picot, N.: DUACS DT2014: the new multi-mission altimeter data set reprocessed over 20 years, Ocean Science, 12, 1067–1090, https://doi.org/10.5194/os-12-1067-2016, 2016.

Qiu, B., Chen, S., Klein, P., Wang, J., Torres, H., Fu, L.-L., and Menemenlis, D.: Seasonality in transition scale from balanced to unbalanced motions in the world ocean, Journal of Physical Oceanography, 48, 591–605, https://doi.org/10.1175/JPO-D-17-0169.1, 2018.

Ray, R. D. and Byrne, D. A.: Bottom pressure tides along a line in the southeast Atlantic Ocean and comparisons with satellite altimetry,
385 Ocean Dynamics, 60, 1167–1176, https://doi.org/10.1007/s10236-010-0316-0, 2010.

Ray, R. D. and Zaron, E.: M_2 internal tides and their observed wavenumber spectra from satellite altimetry, Journal of Physical Oceanography, 46, 3–22, https://doi.org/10.1175/JPO-D-15-0065.1, 2016.

Smith, W. H. F. and Sandwell, D. T.: Global sea floor topography from satellite altimetry and ship depth soundings, Science, 277, 1956–1962, https://doi.org/10.1126/science.277.5334.1956, 1997.

390   Taburet, G., Sanchez-Roman, A., Ballarotta, M., Pujol, M.-I., Legeais, J.-F., Fournier, F., Faugere, Y., and Dibarboure, G.: DUACS DT2018: 25 years of reprocessed sea level altimetry products, Ocean Science, 15, 1207–1224, https://doi.org/10.5194/os-15-1207-2019, 2019.

Tchilibou, M., Gourdeau, L., Lyard, F., Morrow, R., Koch Larrouy, A., Allain, D., and Djath, B.: Internal tides in the Solomon Sea in contrasted ENSO conditions, Ocean Science, 16, 615–635, https://doi.org/10.5194/os-16-615-2020, 2020.

Tchilibou, M., Koch-Larrouy, A., Barbot, S., Lyard, F., Morel, Y., Jouanno, J., and Morrow, R.: Internal tides off the Amazon shelf during two
395   contrasted seasons: interactions with background circulation and SSH imprints, Ocean Science, 18, 1591–1618, https://doi.org/10.5194/os-18-1591-2022, 2022.

Ubelmann, C., Carrere, L., Durand, C., Dibarboure, G., Faugère, Y., Ballarotta, M., Briol, F., and Lyard, F.: Simultaneous estimation of ocean mesoscale and coherent internal tide sea surface height signatures from the global altimetry record, Ocean Science, 18, 469–481, https://doi.org/10.5194/os-18-469-2022, 2022.

400   Vic, C., Naveira Garabato, A. C., Green, J. A. M., Spingys, C., Forryan, A., Zhao, Z., and Sharples, J.: The lifecycle of semidiurnal internal tides over the northern Mid-Atlantic Ridge, Journal of Physical Oceanography, 48, 61–80, https://doi.org/10.1175/JPO-D-17-0121.1, 2018.

Vic, C., Naveira Garabato, A. C., Green, J. A. M., Waterhouse, A. F., Zhao, Z., Melet, A., de Lavergne, C., Buijsman, M. C., and Stephenson, G. R.: Deep-ocean mixing driven by small-scale internal tides, Nature Communications, 10, 2099, https://doi.org/10.1038/s41467-019-10149-5, 2019.

405   Wang, J., Fu, L.-L., Qiu, B., Menemenlis, D., Farrar, J. T., Chao, Y., Thompson, A. F., and Flexas, M. M.: An Observing System Simulation Experiment for the Calibration and Validation of the Surface Water Ocean Topography Sea Surface Height Measurement Using In Situ Platforms, Journal of Atmospheric and Oceanic Technology, 35, 281–297, https://doi.org/10.1175/JTECH-D-17-0076.1, 2018.

Wang, J., Fu, L.-L., Haines, B., Lankhorst, M., Lucas, A. J., Farrar, J. T., Send, U., Meinig, C., Schofield, O., Ray, R., Archer, M., Aragon, D., Bigorre, S., Chao, Y., Kerfoot, J., Pinkel, R., Sandwell, D., and Stalin, S.: On the Development of SWOT In Situ Calibration/Validation
410   for Short-Wavelength Ocean Topography, Journal of Atmospheric and Oceanic Technology, 39, 595–617, https://doi.org/10.1175/JTECH-D-21-0039.1, 2022.

Whalen, C. B., de Lavergne, C., Naveira Garabato, A. C., Klymak, J. M., MacKinnon, J. A., and Sheen, K. L.: Internal wave-driven mixing: governing processes and consequences for climate, Nature Reviews Earth & Environment, https://doi.org/10.1038/s43017-020-0097-z, 2020.

415   Wood, F. J.: The Strategic Role of Perigean Spring Tides: In Nautical History and North American Coastal Flooding, 1635-1976, Department of Commerce, National Oceanic and Atmospheric Administration, National Ocean Survey, 1978.

Wunsch, C.: Internal tides in the ocean, Rev. Geophys. Space Phys., 13, 167–182, 1975.

Zaron, E. D.: Baroclinic tidal sea level from exact-repeating mission altimetry, Journal of Physical Oceanography, 49, 193–210, https://doi.org/10.1175/JPO-D-18-0127.1, 2019.

420   Zhao, Z.: Internal tide radiation from the Luzon Strait, Journal of Geophysical Research: Oceans, 119, 5434–5448, https://doi.org/10.1024/2014JC010014, 2014.

Zhao, Z.: Internal tide oceanic tomography, Geophysical Research Letters, 43, 9157–9164, https://doi.org/10.1002/2016GL070567, 2016.

Zhao, Z.: Southward internal tides in the northeastern South China Sea, Journal of Geophysical Research: Oceans, 125, e2020JC01 654, https://doi.org/10.1029/2020JC016554, 2020.

425   Zhao, Z.: Seasonal mode-1 M_2 internal tides from satellite altimetry, Journal of Physical Oceanography, 51, 3015–3035, https://doi.org/10.1175/JPO-D-21-0001.1, 2021.

Zhao, Z.: Satellite estimates of mode-1 M_2 internal tides uisng nonrepeat altimetry missions, Journal of Physical Oceanography, 52, 3065–3076, https://doi.org/10.1175/JPO-D-21-0287.1, 2022a.

Zhao, Z.: Development of the Yearly Mode-1 M_2 Internal Tide Model in 2019, Journal of Atmospheric and Oceanic Technology, 39, 463 –
430   478, https://doi.org/10.1175/JTECH-D-21-0116.1, 2022b.

Zhao, Z. and Alford, M. H.: New altimetric estimates of mode-1 M_2 internal tides in the central North Pacific Ocean, Journal of Physical Oceanography, 39, 1669–1684, https://doi.org/10.1175/2009JPO3922.1, 2009.

Zhao, Z., Alford, M. H., Girton, J. B., Rainville, L., and Simmons, H. L.: Global observations of open-ocean mode-1 M_2 internal tides, Journal of Physical Oceanography, 46, 1657–1684, https://doi.org/10.1175/JPO-D-15-0105.1, 2016.